Enhanced Spin Injection in Molecularly Functionalized Graphene via Ultrathin Oxide Barriers

J. C. Toscano-Figueroa,[1,2,‡] N. Natera-Cordero,[1,2,‡] D. A. Bandurin,[1,‡,§] C. R. Anderson,[1]
V. H. Guarochico-Moreira,[1,3] I. V. Grigorieva,[1,*] and I. J. Vera-Marun[1,†]

[1] *Department of Physics and Astronomy, University of Manchester, Manchester, United Kingdom*
[2] *Consejo Nacional de Ciencia y Tecnología (CONACyT), México*
[3] *Departamento de Física, Escuela Superior Politécnica del Litoral, Ecuador*

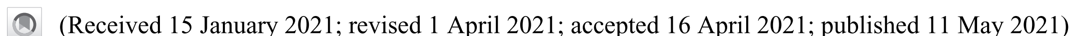
(Received 15 January 2021; revised 1 April 2021; accepted 16 April 2021; published 11 May 2021)

The realization of practical spintronic devices relies on the ability to create and detect pure spin currents. In graphene-based spin valves, this is usually achieved by the injection of spin-polarized electrons from ferromagnetic contacts via a tunnel barrier, with Al_2O_3 and MgO used most widely as barrier materials. However, the requirement to make these barriers sufficiently thin often leads to pinholes and low contact resistances, which, in turn, results in low spin-injection efficiencies, typically 5% at room temperature, due to the so-called resistance mismatch problem. Here, we demonstrate an alternative approach to fabricate ultrathin tunnel-barrier contacts to graphene. We show that laser-assisted chemical functionalization of graphene with sp^3-bonded phenyl groups effectively provides a seed layer for the growth of ultrathin Al_2O_3 films, ensuring smooth high-quality tunnel barriers and an enhanced spin-injection efficiency. Importantly, the effect of functionalization on spin transport in the graphene channel itself is relatively weak, so that the enhanced spin injection dominates and leads to an order of magnitude increase in spin signals. Furthermore, the spatial control of functionalization using a focused laser beam and lithographic techniques can, in principle, be used to limit functionalization to contact areas only, further reducing the effect on the graphene channel. Our results open a route towards circumventing the resistance mismatch problem in graphene-based spintronic devices based on easily available and highly stable Al_2O_3 and facilitate a step forward in the development of their practical applications.

DOI: 10.1103/PhysRevApplied.15.054018

I. INTRODUCTION

Interest in low-dimensional spintronics has intensified during the last decade, following the demonstration of graphene as a truly two-dimensional spin channel [1] exhibiting long spin-relaxation lengths at room temperature [2,3]. Graphene also offers gate-tunable carrier concentration and high mobility, which makes it ideal for the creation of spin-based electronic devices, such as transistors and logic gates [4,5]. An essential part of such devices is a tunnel barrier for spin injection that ideally should be uniform and atomically thin, to achieve an optimum combination of a sufficiently high resistance and a high enough tunneling current [1,6]. Traditionally used tunnel barriers are based on thin oxide films, such as Al_2O_3 and MgO [1,6,7]. These are grown via electron-beam evaporation and typically exhibit spin-injection efficiencies at room temperature of about 5% [3,8]. Similar efficiencies are obtained for Al_2O_3 grown via atomic layer deposition [9]. One of the reasons for such relatively low spin-injection efficiency is the presence of pinholes, as they cause direct ohmic contact and a great suppression of spin polarization due to a fundamental limitation known as the resistance mismatch [10]. The latter limits spin-injection efficiency when the (spin) resistance of an injector contact, R_c, is lower than the typically high spin resistance of the graphene channel, $R^s_{\mathrm{ch}} = \rho\lambda_s/W$ (here, ρ is the sheet resistance of graphene, W the width of the channel, and λ_s its spin-relaxation length) [2]. This results in contact-induced spin relaxation, which greatly decreases the measured spin signals and reduces the spin-relaxation time [11].

Therefore, it is essential to limit the formation of pinholes in ultrathin tunnel barriers. Sputter deposition, a standard industrial method to grow barriers for tunnel magnetoresistance structures, is shown to result in a nearly-pinhole-free about 1-nm-thick Al_2O_3 barrier on graphene [12,13]. However, this method destroys the

*Irina.V.Grigorieva@manchester.ac.uk
†Ivan.VeraMarun@manchester.ac.uk
‡These authors contributed equally to this work.
§Present address: Department of Physics, Massachusetts Institute of Technology, Cambridge, Massachusetts 02139, USA.

 © 2021 American Physical Society

structural integrity of the graphene channel, even leading to its amorphization in the case of MgO deposition. More successful is an alternative approach that involves the fabrication of MgO barriers using a Ti seed layer and making the contacts very narrow (approximately 50 nm wide); this yields a spin-injection efficiency of up to 30% [6]. Another method involves the initial evaporation of Co/MgO electrodes on a SiO_2 substrate, followed by mechanical transfer of a graphene-hexagonal boron nitride (*h*-BN) stack on top of these electrodes, leading to suppression of contact-induced spin relaxation [14]. However, no similar successes are reported for Al_2O_3 barriers. Other efforts to increase the polarization of injected electrons in graphene include using barriers based on functionalized graphene with fluorine [15], amorphous carbon [16], and strontium oxide [17]. Two-dimensional crystals, such as *h*-BN, can act as ideal ultrathin tunnel barriers themselves [18] and are used to demonstrate efficient spin injection in graphene devices [19,20]. Nevertheless, the practical implementation of the latter approach depends on overcoming the formidable challenge of scaling up the identification and mechanical transfer of such ultrathin *h*-BN layers.

Here, we show that the problem of resistance mismatch can be circumvented by the functionalization of designated graphene regions using a photoactivated chemical reaction and subsequent deposition of oxide tunnel contacts. To this end, we demonstrate a controlled and reproducible introduction of sp^3 defects into monolayer graphene using a chemical reaction with benzoyl peroxide (BPO). The reaction can be easily and reliably controlled by irradiation with laser light, with the defect density being determined by the exposure. Functionalization introduces topographic roughness of the graphene surface, which, in turn, leads to a more uniform formation of insulating tunnel barriers. The resulting devices are characterized by an increased spin-tunneling polarization without a significant suppression of the spin-transport parameters in the channel. Our approach offers a convenient and easily scalable method for the development of graphene spintronics with improved spin-injection efficiency.

II. MOLECULAR FUNCTIONALIZATION OF GRAPHENE

To achieve functionalization, we follow the process reported in Ref. [21], where a photochemical reaction between BPO solution and graphene is used to introduce spatially localized defects into the basal plane of graphene. As demonstrated previously, on contact with the solution, BPO molecules efficiently physisorb on the surface of graphene [22] and can subsequently be broken up to form sp^3 bonds with graphene on exposure to laser light [21,23]. The BPO molecules consist of two benzene rings connected by an oxygen bridge; laser radiation breaks up the bridge, producing highly reactive phenyl radicals that covalently bond to graphene, effectively playing the role of "adatoms," as each radical bonds with just one carbon atom [21]. To initiate the functionalization reaction, we use a focused laser beam (532 nm wavelength). The extent of functionalization (the average density of covalently attached phenyl radicals) is controlled by varying the radiation power, P_R, and the exposure time (see the Supplemental Material for further details [24]).

Figure 1(b) shows an optical photograph of a typical graphene flake that is processed by the protocol described above. After the reaction, the flake exhibits no visible changes in optical microscopy, but Raman spectroscopy reveals a modification of the crystal structure, which is apparent from the rise and evolution of D and D' bands upon increasing the exposure during functionalization [Fig. 1(d)]. The emergence of these Raman bands indicates the presence of point defects in the graphene lattice, while their relative intensity ratio ($I_D/I_{D'}$) can serve as a tool to probe the defect type. Previous studies [25] have established that sp^3 hybridization of otherwise flat sp^2-graphene bonds results in $I_D/I_{D'} \sim 13$, a value close to that found in our experiments. This is consistent with the expected sp^3 character of the $\mathrm{C-C}$ bonds between graphene and phenyl radicals [21]. Similarly, the ratio of D and G bands (I_D/I_G) in the Raman spectra provides information on the average density of the introduced defects [25]. We find that I_D/I_G can be controlled within a range of 0–2 by varying the exposure during functionalization, as is apparent from the I_D/I_G ratio mapped onto differently exposed areas of the flake [Fig. 1(b)]: different regions correspond to different radiation power densities from the laser beam, P_R. For the areas with most exposure, the I_D/I_G ratio exceeds unity [see inset of Fig. 1(d)]. For example, a radiation power density of $P_R \sim 5\ \mathrm{mW}/\mu\mathrm{m}^2$ translates to high functionalization and about 0.01% defect coverage, i.e., about 5×10^{11} defects/cm^2 (see Ref. [25] for details of calculating the defect density from Raman spectra).

To verify that the laser-assisted BPO-graphene reaction introduces only adatom-type sp^3 defects (rather than, for example, carbon vacancies) and is reversible, we have performed additional experiments where functionalized graphene flakes are annealed at 300 °C for 3 h under an inert Ar atmosphere. This leads to a strong suppression of the D and D' peaks in the Raman spectra, as shown in Fig. S1 within the Supplemental Material [24], i.e., to the removal of defects. We note that this is only possible for adatoms, as the annealing temperature used is too low to "heal" vacancies [26] (see the Supplemental Material for further details [24]).

For further analysis, we examine the graphene surface using atomic force microscopy (AFM) and analyze the roughness of the flakes. The latter is usually quantified by a root-mean-square (rms) parameter, which provides a measure of the average height variation of the

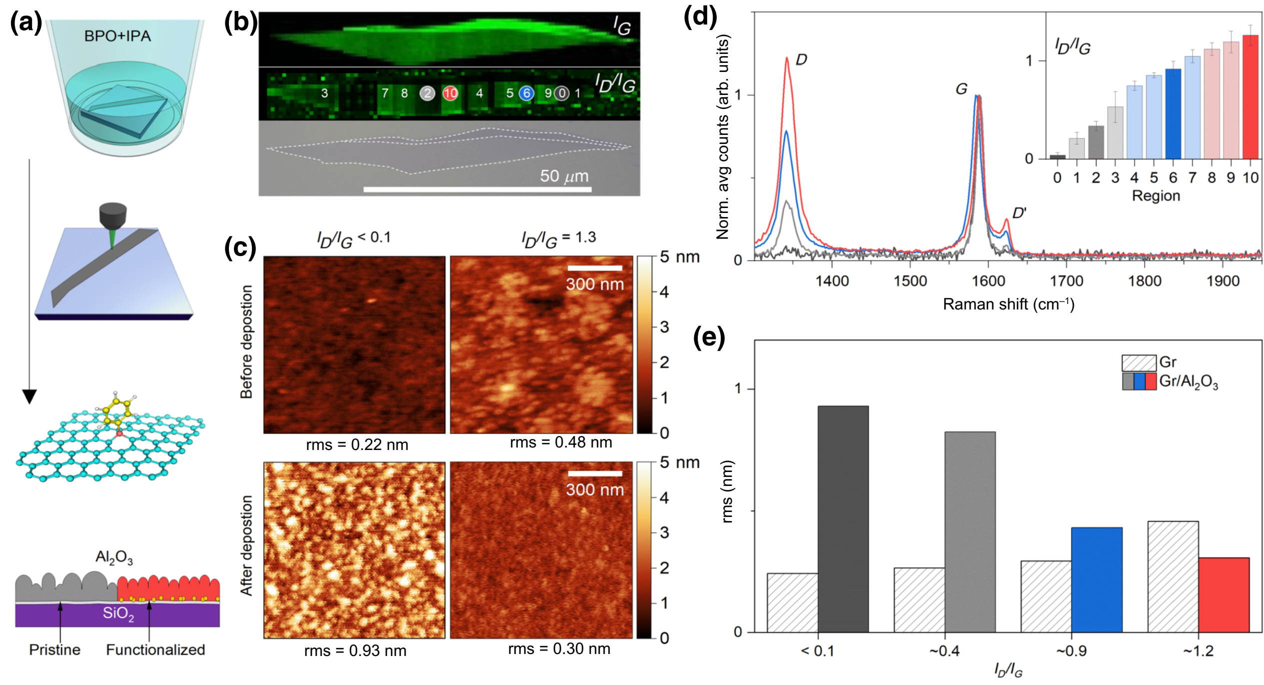

FIG. 1. Controlled functionalization of monolayer graphene and its effect on the growth of an Al_2O_3 barrier. (a) Schematic representation of the functionalization process (top to bottom), with the resulting Al growth morphology (bottom). (b) Raman maps of the *G* peak (top), *D*/*G* intensity ratio (middle), and corresponding optical image of the graphene flake (bottom). Different regions correspond to different laser irradiation doses. Larger outlined area in the optical image is the monolayer. (d) Typical Raman spectra corresponding to regions 0 (black), 2 (gray), 6 (blue), and 10 (red) in (b). Inset, I_D/I_G ratio for all functionalized regions in (b). (c) AFM images of the areas of graphene with lowest (region 0) and highest (region 10) densities of sp^3 defects (top row) and of the same areas after deposition and oxidation of Al (bottom row). (e) Roughness of the oxide film on top of graphene areas with different degrees of functionalization (colored bars) and of graphene prior to Al deposition (hatched bars). Degree of functionalization is indicated by the I_D/I_G ratio.

sample under study. As shown in Fig. 1(c), we find that nonfunctionalized graphene areas exhibit small rms values, typically about 0.2 nm, which are comparable to that of the underlying SiO_2. In contrast, functionalized regions are characterized by a much larger rms value of about 0.5 nm, pointing to their morphological modification by the sp^3-bonded phenyl radicals.

III. TUNNEL-BARRIER MORPHOLOGY AND ELECTRON TRANSPORT

For the purpose of the present study, after functionalization, we deposit 0.6 nm of aluminum and allow its complete oxidation in a controlled O_2 environment. After deposition, we repeat the rms analysis and find that the Al_2O_3 layer formed over functionalized graphene areas is much smoother, with a rms value of only 0.3 nm. This is to be compared with the Al_2O_3 barrier grown on pristine graphene areas that exhibit more than 3 times higher rms. This has proved to be a consistent trend when analyzing different degrees of functionalization, as shown in Fig. 1(e). Although the finding that rougher graphene leads to smoother Al_2O_3 films may seem counterintuitive, it is, in fact, in agreement with expectations, if we recall that deposited metal atoms are known to be highly mobile on pristine graphene [6,27], which leads to significant nonuniformities and/or roughness of ultrathin films. Making graphene less smooth suppresses the high surface diffusion of the metal, resulting in smooth uniform films. Further details of our surface roughness analysis are given in the Supplemental Material [24].

An improved uniformity of the tunnel barriers turns out to be the key parameter ensuring efficient spin-injection, as we now proceed to demonstrate. To this end, we have fabricated several graphene spin valves with several regions of different extents of functionalization. Ferromagnetic Co electrodes are deposited on top of Al_2O_3, to form magnetic tunnel contacts. Each functionalized area is endowed with at least a pair of tunnel contacts [Fig. 2(a)], which allows systematic analysis. Three-terminal measurements of the junctions' contact resistance, R_c, show that it is always greater in the functionalized areas, as compared with pristine (unexposed to laser light) regions [Fig. 2(c)]. For example, the product of R_c and the contact area, A, reaches 100 k$\Omega/\mu m^2$ in the heavily functionalized tunnel junctions, which is an increase of more than 100

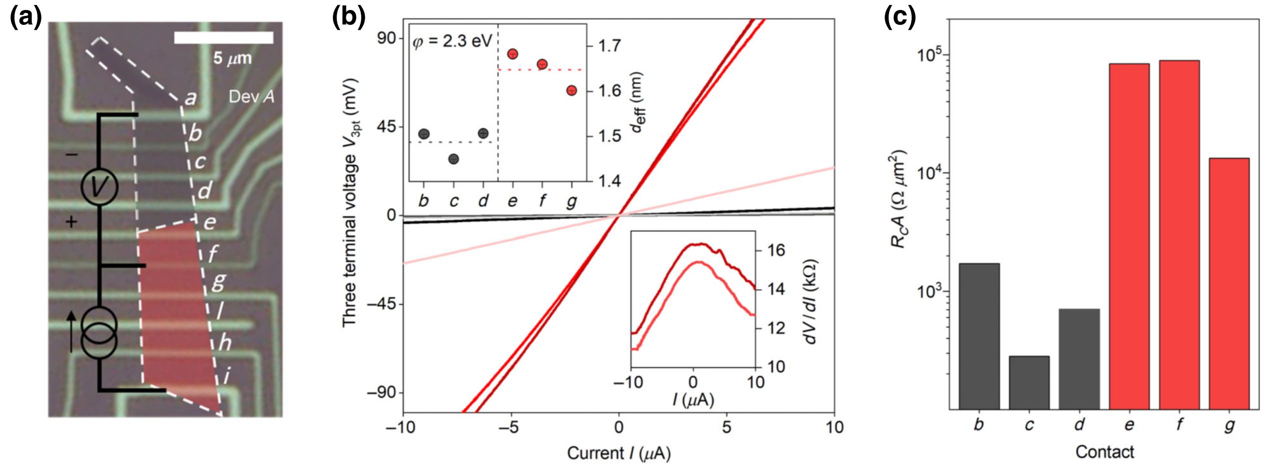

FIG. 2. Effect of functionalization on contact resistance. (a) Optical image of device A; dashed line delimits the regions of the graphene channel that are exposed to laser light at high power density (bottom part) and those only exposed to BPO, but not to laser light (top part). Corresponding I_D/I_G ratios are 0.1 and 1.9. (b) I-V curves for contacts e–g in the highly functionalized region (red curves) and b–d in the unexposed region (gray curves) measured in a three-terminal configuration shown in (a). Left inset, effective tunnel barrier thickness estimated using the Simmons model (see the Supplemental Material [24]). Right inset, differential resistance for contacts e and f, clearly showing nonlinear dependence on the current. (c) Resistance-area product for contacts b–g. Bars are colored red for contacts in the highly functionalized region and dark gray for unfunctionalized graphene.

times compared with Al_2O_3/Co contacts grown on pristine graphene, where R_cA is typically below 1 kΩ/μm^2.

Consistent with the high contact resistance for heavily functionalized areas of graphene, the three-terminal I-V curves exhibit the clear nonlinear behavior shown in Fig. 2(b). This nonlinearity is more apparent on the derivative plots of the I-V curves, which reveal a clear signature of the tunneling behavior: dV/dI decreases with increasing I. In contrast, I-V curves measured on the pristine graphene regions remain linear (ohmic) over the entire I range probed, suggesting the presence of pinholes in the Al_2O_3 barrier. Using the Simmons model [28] to fit the measured I-V curves for heavily functionalized areas, we are able to estimate an effective tunnel-barrier thickness, d_{eff}, and the height of the energy barrier, $\varphi = 2.3$ eV (the latter is in good agreement with the literature [29]). The above φ value is then used to determine the effective barrier thickness for linear I-V curves, such as black and gray curves in Fig. 2(b). See the Supplemental Material for further details of our fitting procedure [24]. The inset of Fig. 2(b) compares d_{eff} for the defect-seeded tunnel junctions and pristine areas: there is a clear increase of d_{eff} in the functionalized areas, particularly for the larger R_cA (contacts e and f).

IV. NONLOCAL SPIN TRANSPORT

For further analysis, we perform standard measurements of the nonlocal resistance, R_{NL}, as a function of in-plane magnetic field, $B_{||}$ [see Fig. 3(a) for the measurement configuration]. This shows a pronounced switching behavior, which is consistent with magnetization reversal of the magnetic electrodes [3,5] and propagation of the pure spin current along the functionalized graphene areas, suggesting a weak effect of functionalization on the spin transport. Furthermore, the change in the nonlocal signal, ΔR_{NL}, between parallel and antiparallel magnetization states reaches values in the range of 20–30 Ω, which is at least an order of magnitude larger than typical values for tunnel junctions grown on pristine graphene and is comparable to state-of-the-art graphene spin valves reported so far [6]. The width of the channel in our devices is in the range of 1–3 μm. Note that, wider devices, e.g., using CVD graphene, with similar polarizations would exhibit correspondingly smaller signals. Changing the direction of the applied magnetic field to be perpendicular to the graphene channel results in Larmor spin precession and further dephasing, also known as a Hanle curve. This leads to a sign reversal of R_{NL} vs $B_\perp$ when the electronic spin accumulation undergoes a π precession [Fig. 3(c)]. Fitting the measured R_{NL} ($B_\perp$) to a standard solution of the Bloch equation allows us to extract the spin-diffusion properties of the device: spin-relaxation length, λ_s; spin-diffusion coefficient, D_s; and effective spin polarization, P_{eff}. Figure 3(e) shows the last two characteristics for different regions within the same device: pristine (i.e., unexposed to laser light) with $I_D/I_G < 0.1$, and heavily functionalized, $I_D/I_G = 1.9$. As one can see from this direct comparison within a single graphene flake, heavily functionalized regions demonstrate a substantial increase of P_{eff}, up to threefold, compared with the unfunctionalized areas, pointing to an improved spin-injection efficiency of the defect-seeded tunnel junctions. Functionalization also leads to an overall enhanced performance of the spin-valve

devices. This is evident in Fig. 3(f), where the nonlocal spin signal for regions with high functionalization is more than an order of magnitude larger than for unfunctionalized areas of the same device.

To elucidate the role of the magnetic tunnel contacts, Fig. 3(f) presents the spin signal as a function of the ratio of the contact resistance, R_c, to the spin resistance of the graphene channel, R^s_{ch}. Within the well-established model by Takahashi and Maekawa [30], both of these resistances act as parallel channels for spin transport. Therefore, R_c/R^s_{ch} represents the ratio of injected spins that continue diffusing and eventually relax inside the graphene channel, to those spins that are reabsorbed by the magnetic electrode, where they rapidly relax, making this ratio a good figure of merit for the effect of relaxation induced by invasive contacts [11,31]. When $R_c/R^s_{\mathrm{ch}} < 1$, spin transport is considered to occur in a regime of spin-resistance mismatch, where the effective spin-injection efficiency of the magnetic tunnel contacts is reduced. In our devices, graphene regions with low functionalization (or not functionalized at all) are within this regime. On the other hand, for highly functionalized graphene, $R_c/R^s_{\mathrm{ch}} \gg 1$, resistance mismatch is minimized, leading to a large increase in ΔR_{NL}. This difference between unfunctionalized and functionalized regions is found to be consistent and reproducible across all studied devices: the former showing $P_{\mathrm{eff}} \leq 5\%$ and the latter $P_{\mathrm{eff}} = 10\%$–20%. Within the functionalized regions, there is no clear correlation between P_{eff} and the degree of functionalization, but it should be noted that the number of studied devices is too small for statistical analysis.

V. SPIN-INJECTION EFFICIENCY

The observed increase in spin signals for our functionalized devices can, in principle, originate from a different scenario, other than the improvement of the spin-injection efficiency of the contacts. Even in a regime free of spin-resistance mismatch, the spin signal depends on several parameters, as per the expression $\Delta R_{\mathrm{NL}} \propto P^2 \rho \lambda_s e^{-L/\lambda_s}/W$ [30]. In our case, the spin-relaxation length is found to change only weakly with an increasing degree of functionalization, with λ_s in the range between 1 and 1.5 μm for all our devices [see inset of Fig. 3(f)]. Therefore, the increased spin signal cannot be explained by a change in spin-relaxation length. This observation is in agreement with previous work on graphene functionalized with chemisorbed hydrogen, which shows that hydrogenation has little effect on the spin-relaxation length [32], whereas another work has found a suppression of the spin-relaxation length [33]. Unlike the spin-relaxation length, the sheet resistance of graphene is known to be strongly affected by sp^3 defects, as they introduce strong pointlike potentials, which cause significant momentum relaxation. The resulting increase in the sheet resistance should lead to a trivial increase of the spin signal via its linear scaling with ρ [30]. Indeed, we observe such a monotonic increase in ρ with the extent of functionalization [see Fig. 3(d)], where highly functionalized graphene, with $I_D/I_G \sim 2$, exhibits a threefold increase in sheet resistance. Notably, this observation from charge-transport measurements is also consistent with the threefold decrease in spin-diffusion coefficient shown in Fig. 3(e), where D_s is obtained from spin-transport measurements on another device [device A, shown in Fig. 2(a)] with a similar level of functionalization ($I_D/I_G = 1.9$). Such inverse scaling between D_s and ρ is indeed expected for spin transport carried by electrons, in the absence of any dominant electron-electron interactions, e.g., spin Coulomb drag [33,34].

To account for this trivial $\Delta R_{\mathrm{NL}} \propto \rho$ scaling, Fig. 3(f) shows ΔR_{NL} normalized to the sheet resistance of each corresponding graphene region. This allows us to remove the contribution due to the increased momentum scattering in functionalized graphene and focus exclusively on the role of the spin injection and detection efficiency of the contacts. Following Takahashi and Maekawa [30], we model the spin signal for functionalized regions of several devices, where we use the corresponding sheet resistances and spin-relaxation lengths for each region. The results in Fig. 3(f) show that devices with highly functionalized regions exhibit contact polarizations at room temperature in the range of 10–20%. For one of the devices (device A), we are able to compare our data with the Takahashi-Maekawa model for the entire range of R_c/R^s_{ch} [solid line in Fig. 3(f)], which shows good agreement for $P \sim 10\%$ for the intrinsic spin polarization of the contacts [here, the P value corresponds to the effective polarization in Fig. 3(e)]. These results provide clear evidence that the notable enhancement of spin signals in our devices is indeed a consequence of the higher contact resistance and effective polarization, P_{eff}.

In its turn, the increased contact resistance is clearly the result of the much-reduced roughness and the absence of pinholes in our ultrathin Al_2O_3 tunnel barriers. We speculate that the reduced roughness is an indication of finer grains in these polycrystalline films, as the grain size is known to strongly depend on the growth conditions (see, e.g., Refs. [35,36]). To this end, we further analyze the surface morphology through AFM images of the Al_2O_3 films deposited on graphene with and without high levels of functionalization, i.e., with I_D/I_G ratios of <0.1 and 1.3, respectively (see the Supplemental Material for details [24]). This shows that the height distribution in the AFM images for Al_2O_3 films deposited on highly functionalized graphene are significantly narrower than for pristine regions, consistent with the extracted rms values. Similarly, the distribution of the lateral sizes of the "grains" in the AFM images [37–39] for highly functionalized graphene is peaked more sharply and at a lower size than that of the Al_2O_3 film grown on unfunctionalized

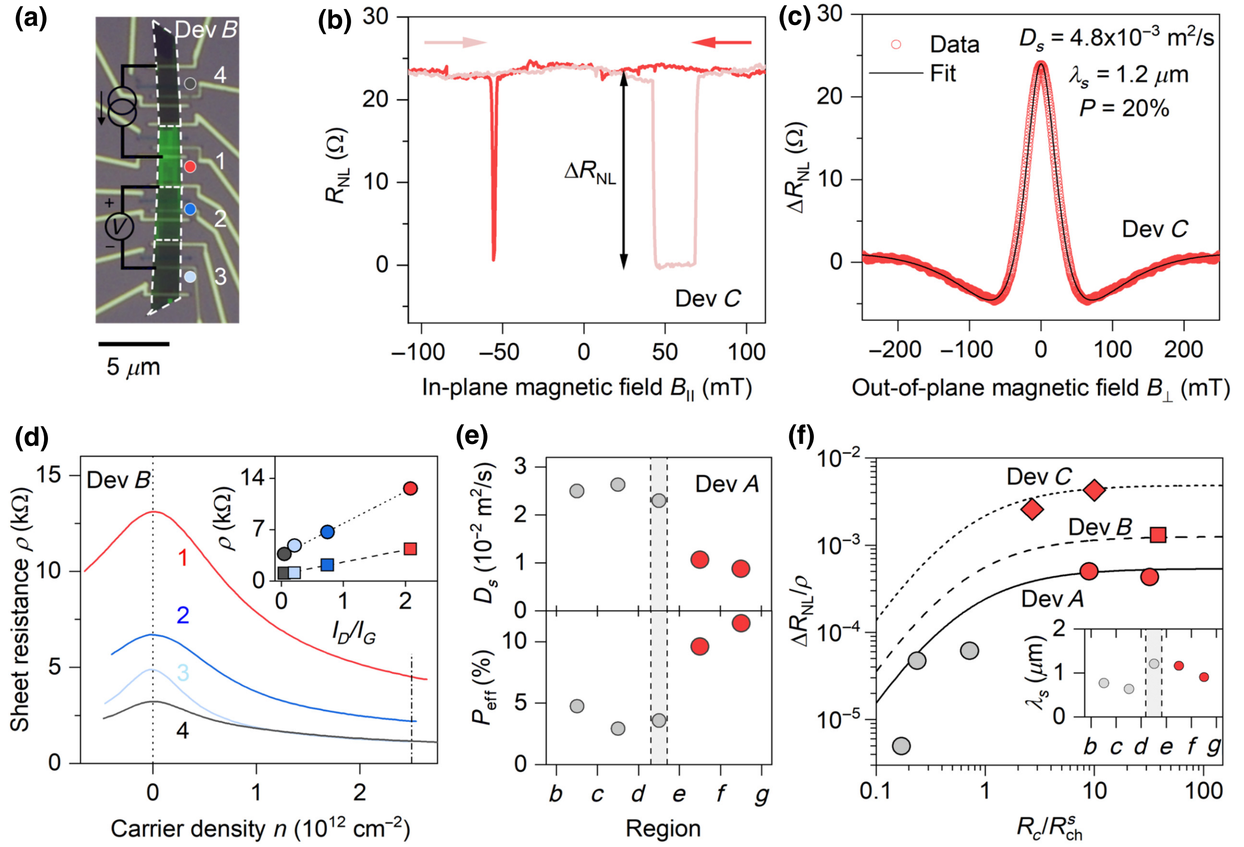

FIG. 3. Spin transport in functionalized graphene and resistance mismatch. (a) Optical image of device B, with four differently functionalized regions (1–4), as indicated by the white-dashed line and a superimposed Raman map showing D/G intensity ratio (ranging from 0 to 2.1). (b) Example of the nonlocal response measured across a highly functionalized area with $I_D/I_G = 1.1$ and $P = 20\%$ in a different device (C). (c) Spin precession (Hanle curve) for the same area as in (b). (d) Resistance vs carrier density for different regions of device B shown in (a). Inset, sheet resistance for the same regions at the neutrality point (circles) and at 2.5×10^{12} cm^{-2} (squares) as a function of the I_D/I_G ratio. (e) Spin-diffusion coefficient and contact polarization obtained from spin-transport experiments for different regions of device A shown in Fig. 2. I_D/I_G ratios are 0.1 (1.9) for gray (red) circles. (f) Scaled nonlocal spin-valve signal vs the ratio of contact resistance to spin-channel resistance, with fits to the Takahashi-Maekawa model (see text). Circular symbols correspond to the same regions from device A as in (e), with the continuous line being the model for $P = 10\%$. Square symbol corresponds to region 1 from device B in (a), with $I_D/I_G = 2.1$ and dashed model line with $P = 9\%$. Diamond symbols correspond to two regions from another device (C, not shown), with $I_D/I_G = 1.1$ and dotted model line with $P = 19\%$. Inset, spin-relaxation length for the same regions as in (e).

graphene. This indicates that sp^3-bonded phenyl groups serve as nucleation centers for Al growth, resulting in smoother oxide films.

The nearly constant spin-relaxation length [inset in Fig. 3(f)] and the decreased diffusion coefficient in our functionalized devices [Fig. 3(e)] imply that the spin lifetime increases as a result of functionalization. This observation is in agreement with previous work on spin transport in graphene functionalized with hydrogen [32], which also reports an enhancement of spin lifetime. As a possible explanation, it is suggested [32] that the increased spin lifetime is consistent with the Dyakonov-Perel (DP) spin-relaxation mechanism: an enhanced scattering by defects in our experiments is indicated by a notable increase of graphene resistance [Fig. 3(d)]. We note that the weak dependence of the spin-relaxation length on the presence of sp^3 defects is in contrast to predictions of Ref. [40], where it is suggested that sp^3 defects should lead to a locally enhanced spin-orbit coupling in graphene, an enhanced spin-flip scattering at defects and a decrease of the spin-relaxation length. However, this prediction does not consider other possible sources of spin-orbit coupling, such as the substrate [41]. In our experiment, the dominant role of defects appears to be related to momentum scattering.

VI. CONCLUSIONS

The proposed laser-assisted BPO functionalization allows the use of thermal evaporation as a deposition technique to achieve tunnel barriers on graphene with both a

large R_cA product and high spin polarization. Evaporation has proven to be beneficial for the fabrication of spintronic devices, as it avoids damage to graphene during deposition, as opposed to sputtering that can also create barriers with a large R_cA product [12], but at the expense of a large defect density in the graphene channel [13]. Furthermore, the possibility of controlling the amount of sp^3 defects in graphene independently of the barrier deposition process creates the possibility of controlling spin transport by utilizing the magnetic nature of sp^3 defects [33,42,43].

Research data are available from the authors upon request.

ACKNOWLEDGMENTS

We acknowledge support from the European Union's Horizon 2020 research and innovation program under Grants No. 696656 and 785219 (Graphene Flagship Core 2) and from the Engineering and Physical Sciences Research Council (UK) EPSRC CDT Graphene NOWNANO EP/L01548X. J.C.T.-F. and N.N.-C. acknowledge support from the Consejo Nacional de Ciencia y Tecnología (México). D.A.B. acknowledges support from the FP7 Marie Curie Initial Training Network "Spintronics in Graphene" (SPINOGRAPH). C.R.A. acknowledges support from the EPSRC Doctoral Training Partnership (DTP). V.H.G.-M. acknowledges support from the Secretaría Nacional de Educación Superior, Ciencia y Tecnología (Ecuador). I.J.V.M. acknowledges support from the FP7 FET-Open Grant No. 618083 (CNTQC).

[1] N. Tombros, C. Jozsa, M. Popinciuc, H. T. Jonkman, and B. J. van Wees, Electronic spin transport and spin precession in single graphene layers at room temperature, Nature **448**, 571 (2007).

[2] I. Zutic, J. Fabian, and S. Das Sarma, Spintronics: Fundamentals and applications, Rev. Mod. Phys. **76**, 323 (2004).

[3] A. Avsar, H. Ochoa, F. Guinea, B. Ozyilmaz, B. J. van Wees, and I. J. Vera-Marun, Colloquium: Spintronics in graphene and other two-dimensional materials, Rev. Mod. Phys. **92**, 021003 (2020).

[4] S. Roche and S. O. Valenzuela, Graphene spintronics: Puzzling controversies and challenges for spin manipulation, J. Phys. D. Appl. Phys. **47**, 094011 (2014).

[5] W. Han, R. K. Kawakami, M. Gmitra, and J. Fabian, Graphene spintronics, Nat. Nanotechnol. **9**, 794 (2014).

[6] W. Han, K. Pi, K. M. McCreary, Y. Li, J. J. I. Wong, A. G. Swartz, and R. K. Kawakami, Tunneling Spin Injection Into Single Layer Graphene, Phys. Rev. Lett. **105**, 167202 (2010).

[7] N. Tombros, S. Tanabe, A. Veligura, C. Jozsa, M. Popinciuc, H. T. Jonkman, and B. J. Van Wees, Anisotropic Spin Relaxation in Graphene, Phys. Rev. Lett. **101**, 046601 (2008).

[8] T.-Y. Yang, J. Balakrishnan, F. Volmer, A. Avsar, M. Jaiswal, J. Samm, S. R. Ali, A. Pachoud, M. Zeng, M. Popinciuc, G. Güntherodt, B. Beschoten, and B. Özyilmaz, Observation of Long Spin-Relaxation Times in Bilayer Graphene at Room Temperature, Phys. Rev. Lett. **107**, 047206 (2011).

[9] T. Yamaguchi, S. Masubuchi, K. Iguchi, R. Moriya, and T. Machida, Tunnel spin injection into graphene using Al_2O_3 barrier grown by atomic layer deposition on functionalized graphene surface, J. Magn. Magn. Mater. **324**, 849 (2012).

[10] G. Schmidt, D. Ferrand, L. W. Molenkamp, A. T. Filip, and B. J. van Wees, Fundamental obstacle for electrical spin injection from a ferromagnetic metal into a diffusive semiconductor, Phys. Rev. B **62**, R4790 (2000).

[11] T. Maassen, I. J. Vera-Marun, M. H. D. Guimarães, and B. J. van Wees, Contact-induced spin relaxation in hanle spin precession measurements, Phys. Rev. B **86**, 235408 (2012).

[12] B. Dlubak, M.-B. Martin, C. Deranlot, K. Bouzehouane, S. Fusil, R. Mattana, F. Petroff, A. Anane, P. Seneor, and A. Fert, Homogeneous pinhole free 1 nm Al_2O_3 tunnel barriers on graphene, Appl. Phys. Lett. **101**, 203104 (2012).

[13] B. Dlubak, P. Seneor, A. Anane, C. Barraud, C. Deranlot, D. Deneuve, B. Servet, R. Mattana, F. Petroff, and A. Fert, Are Al_2O_3 and MgO tunnel barriers suitable for spin injection in graphene?, Appl. Phys. Lett. **97**, 092502 (2010).

[14] M. Drögeler, C. Franzen, F. Volmer, T. Pohlmann, L. Banszerus, M. Wolter, K. Watanabe, T. Taniguchi, C. Stampfer, and B. Beschoten, Spin lifetimes exceeding 12 ns in graphene nonlocal spin valve devices, Nano Lett. **16**, 3533 (2016).

[15] A. L. Friedman, O. M. J. Van 'T Erve, C. H. Li, J. T. Robinson, and B. T. Jonker, Homoepitaxial tunnel barriers with functionalized graphene-on-graphene for charge and spin transport, Nat. Commun. **5**, 3161 (2014).

[16] I. Neumann, M. V. Costache, G. Bridoux, J. F. Sierra, and S. O. Valenzuela, Enhanced spin accumulation at room temperature in graphene spin valves with amorphous carbon interfacial layers, Appl. Phys. Lett. **103**, 112401 (2013).

[17] S. Singh, J. Katoch, T. Zhu, R. J. Wu, A. S. Ahmed, W. Amamou, D. Wang, K. A. Mkhoyan, and R. K. Kawakami, Strontium oxide tunnel barriers for high quality spin transport and large spin accumulation in graphene, Nano Lett. **17**, 7578 (2017).

[18] L. Britnell, R. V. Gorbachev, R. Jalil, B. D. Belle, F. Schedin, M. I. Katsnelson, L. Eaves, S. V. Morozov, A. S. Mayorov, N. M. R. Peres, A. H. Castro Neto, J. Leist, A. K. Geim, L. A. Ponomarenko, and K. S. Novoselov, Electron tunneling through ultrathin boron nitride crystalline barriers, Nano Lett. **12**, 1707 (2012).

[19] M. V. Kamalakar, A. Dankert, J. Bergsten, T. Ive, and S. P. Dash, Enhanced tunnel spin injection into graphene using chemical vapor deposited hexagonal boron nitride, Sci. Rep. **4**, 6146 (2014).

[20] M. Gurram, S. Omar, and B. J. Van Wees, Bias induced up to 100% spin-injection and detection polarizations in ferromagnet/bilayer-hBN/graphene/hBN heterostructures, Nat. Commun. **8**, 248 (2017).

[21] H. Liu, S. Ryu, Z. Chen, M. L. Steigerwald, C. Nuckolls, and L. E. Brus, Photochemical reactivity of graphene, J. Am. Chem. Soc. **131**, 17099 (2009).

[22] G. Gao, D. Liu, S. Tang, C. Huang, M. He, Y. Guo, X. Sun, and B. Gao, Heat-initiated chemical functionalization of graphene, Sci. Rep. **6**, 20034 (2016).
[23] L. Zhang, J. Yu, M. Yang, Q. Xie, H. Peng, and Z. Liu, Janus graphene from asymmetric two-dimensional chemistry, Nat. Commun. **4**, 1443 (2013).
[24] See the Supplemental Material at http://link.aps.org/supplemental/10.1103/PhysRevApplied.15.054018 for more details of the functionalization and its reversibility, device fabrication, electrical characterization, AFM analysis, roughness of SiO_2, and the Simmons model.
[25] A. Eckmann, A. Felten, I. Verzhbitskiy, R. Davey, and C. Casiraghi, Raman study on defective graphene: Effect of the excitation energy, type, and amount of defects, Phys. Rev. B **88**, 035426 (2013).
[26] J. Chen, T. Shi, T. Cai, T. Xu, L. Sun, X. Wu, and D. Yu, Self healing of defected graphene, Appl. Phys. Lett. **102**, 103107 (2013).
[27] C. Binns, S. H. Baker, C. Demangeat, and J. C. Parlebas, Growth, electronic, magnetic and spectroscopic properties of transition metals on graphite, Surf. Sci. Rep. **34**, 105 (1999).
[28] J. G. Simmons, Generalized formula for the electric tunnel effect between similar electrodes separated by a thin insulating film, J. Appl. Phys. **34**, 1793 (1963).
[29] J. S. Moodera and G. Mathon, Spin polarized tunneling in ferromagnetic junctions, J. Magn. Magn. Mater. **200**, 248 (1999).
[30] S. Takahashi and S. Maekawa, Spin injection and detection in magnetic nanostructures, Phys. Rev. B **67**, 052409 (2003).
[31] M. Popinciuc, C. Józsa, P. J. Zomer, N. Tombros, A. Veligura, H. T. Jonkman, and B. J. van Wees, Electronic spin transport in graphene field-effect transistors, Phys. Rev. B **80**, 214427 (2009).
[32] M. Wojtaszek, I. J. Vera-Marun, T. Maassen, and B. J. Van Wees, Enhancement of spin relaxation time in hydrogenated graphene spin-valve devices, Phys. Rev. B **87**, 081402(R) (2013).
[33] K. M. McCreary, A. G. Swartz, W. Han, J. Fabian, and R. K. Kawakami, Magnetic Moment Formation in Graphene Detected by Scattering of Pure Spin Currents, Phys. Rev. Lett. **109**, 186604 (2012).
[34] C. P. Weber, N. Gedik, J. E. Moore, J. Orenstein, J. Stephens, and D. D. Awschalom, Observation of spin Coulomb drag in a two-dimensional electron Gas, Nature **437**, 1330 (2005).
[35] E. M. T. Velu, D. N. Lambeth, J. T. Thornton, and P. E. Russell, AFM structure and media noise of SmCo/Cr thin films and hard disks, J. Appl. Phys. **75**, 6132 (1994).
[36] J. Datta, C. Bhattacharya, and S. Bandyopadhyay, Cathodic deposition of CdSe films from dimethyl formamide solution at optimized temperature, Appl. Surf. Sci. **253**, 2289 (2006).
[37] D. Nečas and P. Klapetek, Gwyddion: An open-source software for SPM data analysis, Cent. Eur. J. Phys. **10**, 181 (2012).
[38] J. Cousty, G. Bertrand, L. Najman, and M. Couprie, Watershed cuts: Minimum spanning forests and the drop of water principle, IEEE Trans. Pattern Anal. Mach. Intell. **31**, 1362 (2009).
[39] P. Klapetek, M. Valtr, D. Nečas, O. Salyk, and P. Dzik, Atomic force microscopy analysis of nanoparticles in non-ideal conditions, Nanoscale Res. Lett. **6**, 514 (2011).
[40] A. H. Castro Neto and F. Guinea, Impurity-Induced Spin-Orbit Coupling in Graphene, Phys. Rev. Lett. **103**, 026804 (2009).
[41] C. Ertler, S. Konschuh, M. Gmitra, and J. Fabian, Electron spin relaxation in graphene: The role of the substrate, Phys. Rev. B - Condens. Matter Mater. Phys. **80**, 041405 (2009).
[42] R. R. Nair, M. Sepioni, I.-L. Tsai, O. Lehtinen, J. Keinonen, A. V. Krasheninnikov, T. Thomson, A. K. Geim, and I. V. Grigorieva, Spin-half paramagnetism in graphene induced by point defects, Nat. Phys. **8**, 199 (2012).
[43] R. R. Nair, I. L. Tsai, M. Sepioni, O. Lehtinen, J. Keinonen, A. V. Krasheninnikov, A. H. Castro Neto, M. I. Katsnelson, A. K. Geim, and I. V. Grigorieva, Dual origin of defect magnetism in graphene and its reversible switching by molecular doping, Nat. Commun. **4**, 2010 (2013).